# Real-time observation of $Cu_2ZnSn(S,Se)_4$ solar cell absorber layer formation from nanoparticle precursors

Roland Mainz,[*a] Bryce Walker,[b] Sebastian S. Schmidt,[a] Ole Zander,[a] Alfons Weber,[a] Humberto Rodriguez-Alvarez,[a‡] Justus Just,[a] Manuela Klaus,[a] Rakesh Agrawal,[b] Thomas Unold[a]

[a] Helmholtz-Zentrum Berlin für Materialien und Energie, Hahn-Meitner-Platz 1, 14109 Berlin, Germany. Fax: +49 30 8062 42931; Tel: +49 30 8062 42210; E-mail: roland.mainz@helmholtz-berlin.de

[b] School of Chemical Engineering, Purdue University, West Lafayette, IN 47906, USA.

‡ Present address: International Iberian Nanotechnology Laboratory, Avenida Mestre Jose Veiga s/n, 4715-330 Braga, Portugal.

## Electronic Supplementary Information

# 1 Experimental Details

## 1.1 Synthesis of nanoparticles

**Material:** Copper (II) acetylacetonate (CuAcac) (99.99% Aldrich), zinc acetylacetonate hydrate powder (ZnAcac) (99.995% Aldrich), tin (IV) bis(acetylacetonate) dibromide (SnAcac) (98% Aldrich), sulfur powder (99.99% Aldrich), hexanethiol (95% Aldrich) and oleylamine (90% Acros Organics) were purchased and used without further treatment.

**Nanoparticle formation:** Quantities of CuAcac, ZnAcac, and SnAcac were dissolved in oleylamine at room temperature to give a final Cu:Zn:Sn atomic ratio of 1.76:1.05:1 respectively, and purged under vacuum at 120°C. The temperature was raised to 225°C where sulfur powder solvated in oleylamine was injected. After 30 minutes the reaction was cooled and washed with hexane, methanol, ethanol, and isopropyl alcohol to remove excess oleylamine. The particles were then suspended in hexanethiol and coated onto molybdenum coated soda-lime glass substrates prepared in house. See also Refs.[1,2]

## 1.2 Reaction chamber

The samples were annealed in a cylindrical graphite reaction box placed inside a vacuum chamber. The reaction box consists of a pyrolytic coated graphite cylinder which is closed by quartz plates at the bottom and at the top. The box is equipped with a motor valve to seal its volume from the atmosphere of the vacuum chamber. The samples and the reaction box were heated by the radiation of eight halogen lamps, four above and four below the reaction box, with a total maximum power of 4 kW. An unavoidable heat up of the sample holder during the annealing processes leads to a vertical shift of the sample position of about 200 µm relative to the reaction chamber. To keep the sample position constant with respect to the active volume, the vertical position of the chamber was corrected by a software controlled feedback loop which analyzes the fluorescence intensities in real-time during the processes.

## 1.3   Selenization processes

During evacuation of the chamber, the valve of the reaction box was left open. After a base pressure of $\sim 10^{-4}$ mbar was reached inside the vacuum chamber, the valve of the reaction box was closed. The samples, the reaction box and the selenium were heated simultaneously by the radiation of the halogen lamps above and below the reaction box. The temperature during the processes was measured and controlled by a thermocouple inside the reaction box placed 5 mm above the sample. We assume the temperature of the film to be within $\pm 30$ °C of the measured temperature during the slow heating process and during the temperature plateau of the fast heating. During the heating ramp of the fast heating process, the temperature of the film is estimated to lag up 100 °C behind the measured temperature. This estimation results from comparisons of measured thermal expansions of lattice plane spacings during slow heating (0.05 K/s) and fast heating (1.7 K/s).

## 1.4   Electron microscopy

EDS measurements were performed in a LEO GEMINI 1530 scanning electron microscope equipped with a Thermo Fisher Scientific X-ray silicon drift detector. The TEM measurements were performed in a Zeiss LIBRA 200FE with an acceleration voltage of 200.0 kV. A Thermo Fisher Scientific X-ray Si(Li) detector was applied for the EDS measurements in TEM. The TEM samples of the cross sections of the Cu-Sn-Zn-Se thin films were prepared by mechanical polishing, followed by Ar ion etching using an acceleration voltage of 3 keV and 9° incident angle.

# 2   Analysis of EDXRD data

## 2.1   Resolution limit of domain sizes from peak broadening

A certain crystallite size (which is the size of a domain of coherent scattering) leads to a certain broadening of the diffraction line profile according to Scherrer's formula[3]. However, also microstrain[4] and compositional inhomogeneities[5,6] may contribute to the broadening of a line profile. This complicates the determination of crystallite sizes. Especially because the contribution by inhomogeneities can have strong effects on the shape of the line profile. Despite these additional possible sources for profile broadening, a lower limit of the crystallite size can be determined from the profile breadth by assuming that all the broadening solely stems from the crystallite size. This means that if the crystallite size was smaller than the value determined with this assumption, the profile would be broader in any case.

The signal measured by the detector is a convolution of the experimental function, which is dominated by the detector with a Gaussian shaped broadening, and the profile of the diffraction line, which - in a first approximation - has a Cauchy shape in the case of line broadening caused by crystallite size. The convolution of Gauss and Cauchy profile gives a Voigt profile. The measured data were fitted by a multipeak-fit using pseudo-Voigt profiles, which is an approximation of the Voigt profile. The accuracy of the fit was increased by averaging ten sequential spectra before fitting.

The broadening caused by the crystallite size can be expressed by the integral Cauchy breadth[7] calculated from the pseudo-Voigt profiles. The crystallite size is correlated with the Cauchy breadth $\beta_C$ via the energy-dispersive Scherrer equation[8]

$$D/k = hc/(2\beta_C \cdot \sin(\theta)) \tag{1}$$

where $D$ is the volume weighted crystallite size which corresponds to the size of a domain of coherent scattering, $k$ the Scherrer constant which is close to one for most crystallite shapes[9], $h$ the Planck constant, $c$ the speed of light, $\beta_C$ the integral Cauchy breadth and $2\theta$ the diffraction angle.

A pseudo-Voigt profile is a linear combination of a Cauchy (also called Lorentz) and a Gaussian profile:

$$PV(E, E_0, w, \eta) = \eta \frac{1}{1 + \left(\frac{E - E_0}{w}\right)^2} \tag{2}$$

$$+ (1 - \eta) \exp\left[-\ln(2)\left(\frac{E - E_0}{w}\right)^2\right]$$

where $2w$ is the FWHM, $E$ the photon energy, and $E_0$ the energy of the maximum of the profile. The Cauchy breadth can be calculated by the parameterization of Delhez et al.:[7]

$$\beta_C \approx \left(a_0 + a_1\phi + a_2\phi^2\right)\beta$$

where $\beta$ is the total integral breadth of a pseudo-Voigt profile

$$\beta(w,\eta) = \left(\pi\eta + (1-\eta)\sqrt{\frac{\pi}{\ln 2}}\right)\cdot w \tag{3}$$

and $\phi = 2w/\beta$, $a_0 = 2.0207$, $a_1 = -0.4803$, $a_2 = -1.7756$.

Since the Gauss contribution to the signal is assumed to only come from the detector function, the Gauss breadth of the pseudo-Voigt profiles was set to the breadth of the detector function and was kept fixed during the peak fits. This restriction significantly increases the fit stability of the multi-peak fit, and at the same time leads to a very good fit of the measured data, as can be seen in Figure 2 in the main text. The Gauss breadth of the detector function as function of the signal energy was determined with a $LaB_6$ reference powder (see Fig. S1).
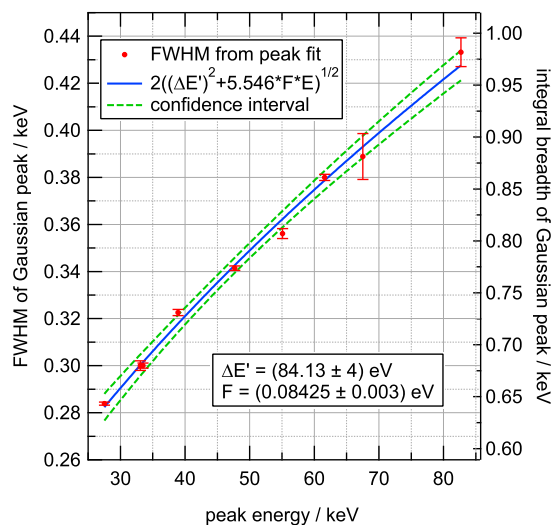


Figure S1: Peak width as function of peak energy determined from an EDXRD measurement of a LaB6 reference powder. The measured data were fitted by the function of Buras[10] $\Delta E_{\mathrm{FWHM}}(E) = 2\sqrt{(\Delta E')^2 + 5.546\cdot F\cdot E}$.

To be able to keep the Gauss breadth constant during the peak fit, the pseudo-Voigt function has to be rewritten to make the Gauss breadth an independent variable. We do this with the help of the parameterization of Delhez et al. for the calculation of the Gauss breadth from the parameters of a pseudo-Voigt function:[7]

$$\beta_G \approx \left(b_0 + b_{1,2}\sqrt{\phi - 2/\pi} + b_1\phi + b_2\phi^2\right)\cdot\beta \tag{4}$$

with $\phi = 2w/\beta$, $b_0 = 0.6420$, $b_{1,2} = 1.4187$ , $b_1 = -2.2043$ , $b_2 = 1.8706$ . With eqs. (4) and (3) we obtain

$$w(\beta_G,\eta) = \frac{\beta_G\cdot\phi}{2\left(b_0 + b_{1,2}\sqrt{\phi - 2/\pi} + b_1\phi + b_2\phi^2\right)}.$$

With this relation, the pseudo-Voigt function (2) can be expressed as a function of $\beta_G$:

$$PV(E,E_0,\beta_G,\eta) = PV(E,E_0,w(\beta_G,\eta),\eta).$$

The broad $\Sigma 1$ signal shown in Fig. 2 of the main part of the paper is symmetric in the initial state and becomes asymmetric during the process. The domain size broadening, however, only causes a symmetric broadening. Therefore, the steeper shoulder determines the lower limit of the crystallite size.

The asymmetry can be explained by an inhomogeneous replacement of sulfur by selenium, which is also observed in the SEM mappings. The real crystallite size may be larger, if the high-energy shoulder of the peak is additionally broadened by composition gradients. The accuracy of the fit was increased by averaging ten sequential spectra before fitting.

## 2.2   Temperature-dependent lattice parameters of CuSe

The hexagonal structure of the phase attributed to CuSe was confirmed by a lattice parameter fit. A fit performed on the data recorded at 320 °C gave the following parameters:

$$a = 0.4013\,\text{nm}, \quad \alpha = 89.6°,$$
$$b = 0.4013\,\text{nm}, \quad \beta = 90.4°,$$
$$c = 1.7282\,\text{nm}, \quad \gamma = 120.5°.$$

It can be seen that the deviations from an ideal hexagonal structure are small. When the constraints for a hexagonal structure ($a = b$, $\alpha = \beta = 90°$, $\gamma = 120°$) are imposed on the lattice parameters, the fit on the same data gives

$$a = 0.3986\,\text{nm},$$
$$c = 1.7281\,\text{nm}.$$

Time-resolved values of the lattice parameters $a$ and $c$ were determined by performing a fit on each recorded spectrum. The resulting lattice parameters and the ratio $c/a$ as functions of process time and temperature are shown in Fig. S2.
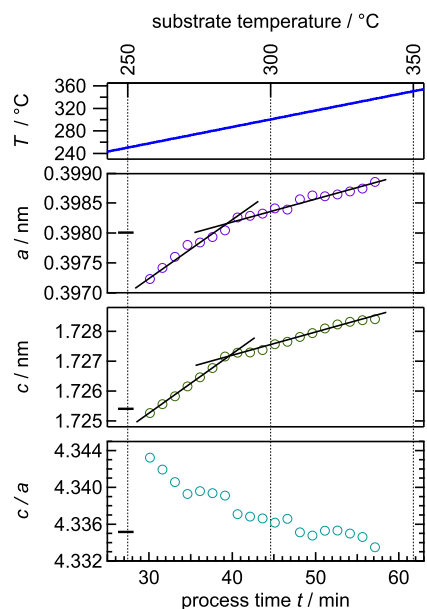


Figure S2:  Time-resolved evolution of the lattice parameters of hexagonal CuSe. For each point in time the lattice parameters were determined by a fit which refines the lattice parameters to match the d-spacings. The short horizontal lines mark the values given in the reference ICDD card no. 86-1240 for a temperature of 242 °C (515 K).

# 3    Transmission electron microscopy

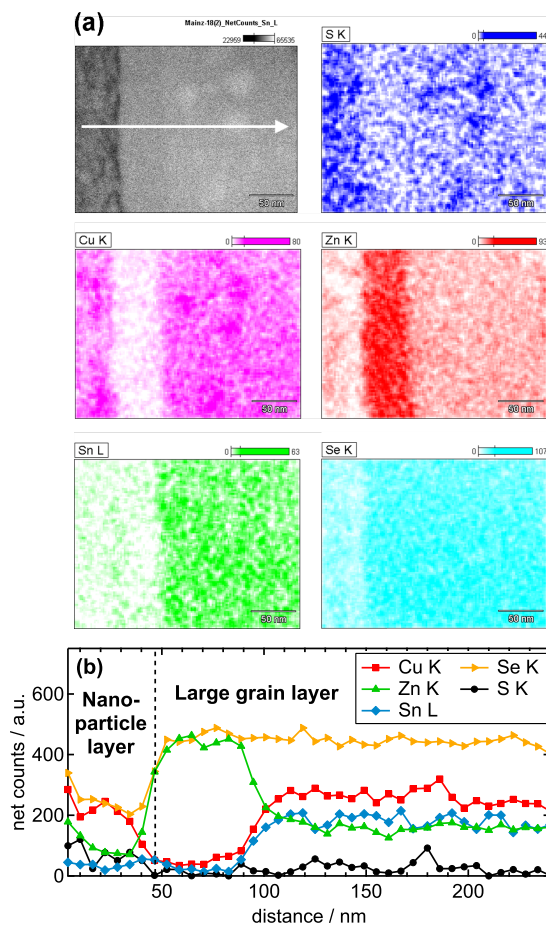**Cross-sectional TEM-EDS analysis of the sample selenized by slow heating to 400°C**



**Figure S3:** (a) TEM-EDX mappings of a region around the interface of the nanoparticle layer and large grained layer of the sample that was selenized by slow heating up to 400°C. In the upper left gray scale image the two distinct layers can be identified, with the nanoparticle layer on the left hand side of the image. (b) Line scan across the interface of the nanoparticle layer and large grained layer. The white arrow in (a) marks the position of the data for the line scan. The position of the zero point of the x-axis in the line scan is arbitrary.

**Cross-sectional TEM-EDS analysis of the sample selenized by fast heating to 500°C**
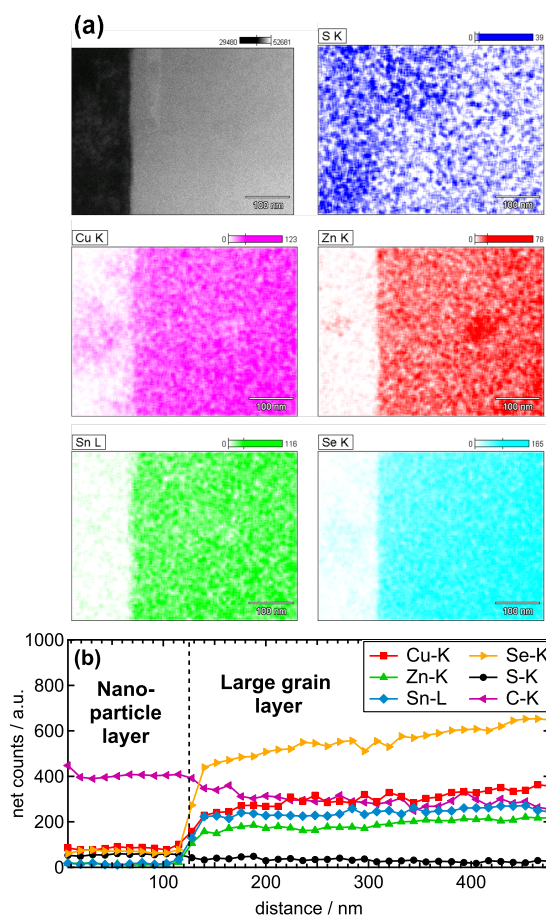


Figure S4: (a) TEM-EDX mappings of a region around the interface of the nanoparticle layer and large grained layer of the sample selenized with fast heating (1.7 K/s) up to 500°C. (b) Line scan across the interface of the nanoparticle layer and large grained layer. The position of the zero point of the x-axis is arbitrary.

# References

1  Q. Guo, H. W. Hillhouse and R. Agrawal, *J. Am. Chem. Soc.*, 2009, **131**, 11672–11673.

2  Q. Guo, G. M. Ford, W.-C. Yang, B. C. Walker, E. A. Stach, H. W. Hillhouse and R. Agrawal, *J. Am. Chem. Soc.*, 2010, **132**, 17384–17386.

3  P. Scherrer, *Nachr. Ges. Wiss. Göttingen,*, 1918, 98–100.

4  D. Apel, M. Klaus, C. Genzel and D. Balzar, *Z. Kristallogr.*, 2011, **226**, 934–943.

5  I. M. Kötschau and H. W. Schock, *J. Appl. Crystallogr.*, 2006, **39**, 683–696.

6  T. Rissom, R. Mainz, C. A. Kaufmann, R. Caballero, V. Efimova, V. Hoffmann and H.-W. Schock, *Sol. Energy Mater. Sol. Cells*, 2011, **95**, 250–253.

7  R. Delhez, T. H. Keijser and E. J. Mittemeijer, *Fresenius. J. Anal. Chem.*, 1982, **312**, 1–16.

8  L. Gerward, S. Morup and H. Topsoe, *J. Appl. Phys.*, 1976, **47**, 822–825.

9  J. I. Langford and A. J. C. Wilson, *J. Appl. Crystallogr.*, 1978, **11**, 102–113.

10  B. Buras, *J. Appl. Crystallogr.*, 1978, **11**, 137–140.